DISCRETE-FREQUENCY INFRARED IMAGING WITH A QUANTUM CASCADE LASER AND DIFFUSE OPTICAL RAMAN TOMOGRAPHY: METHODS TOWARD IMPROVING CLINICALLY RELEVANT LABEL-FREE CHEMICAL CONTRAST

BY

MATTHEW R. KOLE

THESIS

Submitted in partial fulfillment of the requirements
for the degree of Master of Science in Bioengineering
in the Graduate College of the
University of Illinois at Urbana-Champaign, 2012

Urbana, Illinois

Adviser:

Professor Rohit Bhargava

ABSTRACT

Label-free chemical imaging provides the ability to probe chemical structure without interference from dyes or other contrast agents which potentially alter the system being studied. Two emerging, non-invasive spectroscopic methods with significant potential include the use of quantum cascade laser technology for mid-infrared spectral imaging and diffuse Raman tomography for three dimensional chemical analysis. In this thesis, we constructed and evaluated two analytical instruments which represent the first steps toward realizing these technologies. First, a discrete frequency imaging microscope that uses a tunable quantum cascade laser (QCL) source and an uncooled bolometer camera is described. Its performance is compared to a commercial Fourier transform infrared (FT-IR) instrument, and a significant signal to noise advantage over conventional sources was observed when using a spatial filter aperture on the order of the wavelength of light (10μm). We further demonstrate this advantage by illustrating supersampling point mapping which is not achievable with conventional sources. Second, we present experimental results and theoretical considerations for Raman tomography measurements. Using a fiber-coupled Raman spectrometer, spectra were acquired from Teflon spheres embedded in an Intralipid-based tissue-mimicking sample. The instrument's source-detector collection angles were systematically varied to achieve multiple diffuse projections. Two light fluence modeling methods, radiative transport calculation and Monte Carlo simulation, were compared. Reconstruction of the size and position of buried targets was attempted via an iterative modified-Tikhonov minimization algorithm without the use of spatial priors. The accuracy of these reconstructions was validated using computed tomography (CT) images. We found that although radiative transport methods provide a good first approximation for reconstructions, Monte Carlo methods may have a higher capacity for more accurately modeling the propagation of directionalized light sources over short distances (<1cm). This work illustrates a proof of principle for both technologies as well as providing a guide to future instrumentation development.

ACKNOWLEDGEMENTS

I would like to thank my adviser Dr. Rohit Bhargava for his guidance and support, both of which enable me to continue to pursue my interests in the laboratory. I would also like to extend thanks to all of my friends in the Chemical Imaging and Structures Laboratory, especially to Dr. Matthew Schulmerich whose daily mentorship has been invaluable in my development as a scientist. Finally, I would like to thank my parents who have played the most important role of all. I am always grateful for all that you do.

TABLE OF CONTENTS

CHAPTER 1: INTRODUCTION AND MOTIVATION

Chemical imaging represents a powerful set of analytical tools which may be applied to a wide range of scientific and medical problems. One of the greatest strengths of vibrational spectroscopic imaging is that dyes, fluorescent tags, nanoparticles, or other exogenous agents are not required; chemical contrast is endogenous and arises from certain vibrational modes of individual chemical bonds or specific groups of such bonds.[1] This yields several distinct advantages over techniques which use dyes or tags. Sample preparation without a dye or tag interferes less with the chemical integrity of the specimen. Such preparation can also be less costly, less time consuming, and less experimentally complex than contrast agent counterparts, leading to greater experimental throughput. Live cell imaging is readily feasible with certain forms of vibrational imaging,[2] and in this manner the possibility of in vivo measurements can be realized.[3] Additionally, where one contrast agent is required for each structure or compound of interest, vibrational spectroscopy can often monitor many chemical signatures simultaneously. The acquisition of a complete chemical spectrum represents a natural multiplexing advantage, allowing for certain experiments to be carried out in situations where using multiple dyes or tags is not possible. Even with these distinct advantages, there remains much untapped potential in the use of inherent chemical contrast for imaging. The development of vibrational spectroscopies for scientific and medical purposes is still an expanding area of active research.

Cancer diagnosis presents a number of challenges which are particularly well suited to the strengths of vibrational spectroscopy. The current gold standard for diagnosis involves the invasive collection of a tissue biopsy followed by chemical fixation, thin sectioning, and staining.[4] A group of trained pathologists then observes each of the stained sections with a white light microscope and makes a diagnosis. While this method represents the standard of care, there are several facets of this process that could benefit from new technology. As with any examination or test, there is a nonzero rate of error

(false positives and false negatives).[5] Compounding this possibility for error is the fact that diagnosis is subjective to the experiences of the pathologists and physicians. In any decision-making process there is a small but unquantifiable and varying capacity for bias or human error. Any additional information that chemical imaging could provide to the pathologists without interfering with the current clinical workflow could potentially aid in producing correct diagnoses. Furthermore, if chemical imaging techniques could be used to expedite the diagnosis process or make it less painful or costly, the sheer number of biopsies performed each year[6] could lead to a significant decrease in cost, time, or patient stress.

Steps towards realizing vibrational spectroscopy in cancer diagnosis have begun to emerge in recent years. Cell-type classification in fixed biopsy sections using FT-IR (Fourier transform infrared) imaging has been demonstrated.[7] Such a tool could serve to augment the amount of information available to a pathologist without the need for additional tissue quantity or preparation. One highly desirable feature of this technique is that it generates digitized data on which statistical analysis can be readily performed, introducing objectivity into the clinical workflow. Even though chemical imaging of biopsied tissue has been shown to be effective in the laboratory, further development is necessary for widespread clinical use.

In addition to further advances and documentation of precision, accuracy, and robustness, cost is an important concern when the end goal of a project is development for healthcare use. Cost limits a technology's accessibility, and clinical impact can only occur if chemical imaging tools are made accessible. The operational costs of commercial FT-IR instrumentation are not negligible. One of the most critical technologies of such an instrument is the focal plane array (FPA) detector. This device requires a continuous supply of liquid nitrogen to run and may require special training to operate and maintain. Additionally, FT-IR imaging is a time-consuming process. In order to obtain a quality interferogram (leading to a quality absorbance spectrum), multiple scans of a biopsy must be taken. Once a spectrum is obtained, not all frequencies are utilized in classifying cell types.[7] This collection of 'unused' spectral information is unavoidable in FT-IR methods. If a new instrument were developed that could sample only the necessary portions of the infrared absorbance spectrum while increasing scan

speeds and decreasing the number of total scans required, great increases in throughput and efficiency could be realized. This efficiency could mean a reduced instrumentation requirement in clinics and therefore a greatly reduced cost. The development of high signal to noise, non Fourier-transform imaging methods could also benefit laboratory applications where only single-frequency images are required.

Feasibility and impact in the deployment of chemical imaging technologies into the clinic can also be realized by simplifying and streamlining the clinical workflow. One way to achieve this would be through in vivo imaging for 'optical biopsying.' In addition to the obvious benefits of noninvasiveness, circumventing the need to perform some biopsies also has the potential to alter clinical workflow by reducing the need for surgery, tissue preparation, and staining. The ability to probe the chemical structure of tissues or turbid specimens without sectioning or extensive sample preparation could also be useful in a number of scientific applications. This possibility for a streamlined workflow represents another way in which chemical imaging could provide cost-effective and impactful tools in the clinic.

The advancement of new tools for infrared imaging and for probing the chemical makeup of large tissue specimens lend well towards the realization of optical biopsies and noninvasive in vivo disease detection. This manuscript describes two novel instruments, a discrete frequency infrared (DF-IR) microscope which utilizes a quantum cascade laser (QCL) as its primary light source and a Raman tomography system based on the established science of diffuse optical tomography (DOT). Each system addresses issues associated with these two chemical imaging goals and represents steps towards their realization. The first (DF-IR with QCL) evaluates a new infrared source and a simple, low-cost detector as a potential replacement for traditional blackbody sources and expensive focal plane arrays in certain applications. The second (Raman tomography) describes efforts to develop an instrument that maps Raman signal to confined regions of a large (centimeter scale) tissue phantom, representing a step towards the ability to chemically evaluate regions of tissue in vivo.

CHAPTER 2: DISCRETE FREQUENCY INFRARED MICROSCOPY AND IMAGING WITH A TUNABLE QUANTUM CASCADE LASER SOURCE

Section 2.1 Introduction

Due to improvements in the 25 years since its commercial inception,[8] Fourier-transform infrared microscopy (FT-IR) is widely used for chemical mapping and imaging.[9] While imaging is now well established for fast, spatially-resolved spectroscopy,[10,11] existing instruments depend on a combination of multiplexing via interferometry and multichannel detection for high throughput and increasingly rapid scan times.[12,13] The inclusion of multiple-element linear and array detectors has been the principal driving force for widefield modalities of FT-IR microscopy.[14] While these detector improvements have resulted in tremendous progress, with notable exceptions,[15,16] instruments use an interferometer coupled with a thermal illumination source. This setup is exceptionally efficient, stable and commercially successful; however, practitioners have to acquire a large bandwidth of data even if they are interested in only a small set of wavelengths. A smaller set has been shown to be particularly useful in tissue classification[7] or for monitoring dynamic processes in polymers.[17] Techniques which save time by probing only these wavelengths may facilitate rapid data acquisition and analyses. As opposed to FT-IR spectroscopic methods, measurements of a few selected spectral features may be termed discrete frequency IR (DF-IR) spectroscopy methods. One straightforward approach to DF-IR spectroscopy and imaging may be to use a grating.[15] The use of a dispersive or scanning monochromator for infrared microscopy instrumentation is uncommon due to the inherent low blackbody illumination intensity at individual wavelengths. Additionally, Jacquinot's advantage as well as the spectral multiplexing (Fellgett) advantage are forfeited.[18] In imaging, the multiplexing advantage may be recovered somewhat[15] by using an array detector, but a configuration in which the array is simultaneously used for both spectral and spatial measurements compromises the imaging potential. While sources such as a synchrotron can potentially

provide the flux to overcome the throughput disadvantage, a recent emphasis in the use of synchrotrons has been to utilize this source brightness to instead perform high-resolution imaging,[19,20] which in turn would not provide sufficient flux for appreciable non-multiplexed methods. Narrowband filters may enable both widefield imaging and DF-IR spectroscopy but are only now maturing as a technology and feature intensities limited by the coupled broadband source.[21]

Recently, narrow-bandwidth quantum cascade lasers (QCLs) have become available. In their most common implementation, QCLs are tunable, external-cavity mid-infrared lasers with high power outputs and grating-assisted spectral selection. First developed in the 90s,[22] these devices have been previously used in the detection of trace particles in gasses,[23] wavelength-modulation absorption measurements,[24] and in photoacoustic spectroscopy.[25] Early QCLs featured too limited a spectral range and too wide a bandwidth to be useful for general spectroscopic analyses. At present, QCLs are being developed that have large tunable ranges and spectral linewidths on the order of or smaller than the narrowest absorption bands in condensed phase materials. While the tunable range of individual QCLs still covers only a small region of the mid-IR spectrum (for example, here we use a QCL over the range 980-1204 cm^{-1}), these devices represent emerging sources with broad tunable ranges, high-power, and narrow-bandwiths which are suitable for mid-IR spectroscopy. Additionally, these characteristics may render these new lasers suitable as sources for discrete frequency infrared spectroscopy and microscopy. The use of QCLs for IR microspectroscopy and imaging has been proposed and demonstrated.[26,27] It is presently unclear whether QCLs offer a microscopy advantage over FT-IR imaging and what specific advances may be enabled by the higher flux. In this manuscript, we describe the use of a QCL as a source in infrared widefield imaging and point-mapping. By coupling the bright source to an infrared microscope, we take advantage of the laser's high power to perform imaging in a DF mode and compare the results to FT-IR imaging. We also examine whether a low-cost bolometer can be used as a widefield detector alternative to the current standard of expensive liquid-nitrogen cooled detectors. Further extending attainable data quality, we examine the possibility for high resolution point mapping based on recent theory[28] using a

micrometer-sized aperture. As QCLs are a coherent source, we describe the implications of this property with regards to imaging.

Section 2.2 Instrumentation and Methods

Instrumentation

The instrumentation, set up in-house, consists of three main components: a narrow-bandwidth QCL laser (Daylight Solutions, San Diego, CA), an infrared microscope (Varian Inc., Palo Alto, CA), and detectors. Two detectors were used - a microbolometer camera with a 324 by 256 pixel chip, pixel size 38x38 μm (Photon series, FLIR, Boston, MA), and a liquid nitrogen cooled single element mercury cadmium telluride (MCT) detector (InfraRed Associates, Stuart, FL). For widefield imaging, the output beam from the QCL was expanded 10:1 (from a 6mm beam diameter to approximately 60mm) via two gold-coated parabolic mirrors. The expanded beam was passed through an iris and entered the side port of the infrared microscope. In transmission mode, the beam was condensed through a 0.5 NA Schwarzchild objective lens before passing through the sample stage. The beam exiting the sample stage was collected using a matched 15X Schwarzchild reflecting objective. The image was then passed through the microscope's open aperture and imaged onto the bolometer using another Schwarzchild lens. For point mapping measurements, the same configuration was used but apertures of variable opening were placed in the beam path after the sample to restrict light to be from a defined spatial region of the sample. Beam expansion optics were removed, and the single element detector was also used in place of the array detector. A 74x reflecting objective was utilized instead of one of the matched Schwarzchild objectives.

Certain portions of the experiment called for the use of a rotating diffuser plate consisting of a one inch diameter, scratched calcium fluoride plate and a small motor. When in use, it was placed between the second parabolic mirror and the iris, after beam expansion but before the microscope entrance. With the rotating diffuser in place, 64 sequential frames were acquired for each wavelength. These were averaged

in order to correct for the changing position of the plate. Single frames were acquired for images without the diffuser. While this affects the signal to noise ratio of the data, we do not consider this aspect here as our focus was on obtaining imaging contrast.

A commercial FT-IR imaging spectrometer (Spotlight 400, Perkin Elmer, Waltham, MA) was also used as a performance standard to compare with the instrument described above. The spectrometer was operated in rapid scan mode at a mirror speed of 2 cm/s. Data were acquired over the 7200-0 cm^{-1} range and truncated to 4000-720 cm^{-1} range of interest. N-B medium apodization was used for spectral transformation and a suitable background was acquired from a region adjacent to the sample.

Data Acquisition and Processing

The test sample in this manuscript was a USAF 1951 optical resolution (bar) target fabricated in-house. Briefly, during the fabrication process, uncured SU-8 photoresist resin was spin coated to a desired thickness, cured, post-baked and solvent developed. The target is evaluated using optical microscopy to confirm geometric fidelity. Elements 5 and 6 of cycle 3 were imaged in all instances. All image processing was performed in ENVI (ITT Visual Information Solutions, Boulder, CO) and Matlab (The MathWorks, Nantucket, MA) using code written in-house. Single-beam images had no correction applied, while absorbance images had been divided by a reference image consisting of an unmodified barium fluoride disk. Images taken at discrete frequencies with the QCL and the bolometer also have a 'dark current' chip image subtracted from both the single-beam and background images.

Section 2.3 Results and Discussion

The optical microspectroscopy and imaging configurations to conduct the experiments described in this manuscript were set up. A schematic of the two major setups is shown in Figure 2.1. These flexible configurations allowed us to perform a number of experiments by changing certain aspects of the optical

train as needed to understand the different effects associated with using QCLs. For this preliminary study, we chose to image a USAF 1951 optical resolution bar target, which has historically been used a standard for measuring the performance of optical and IR imaging instrumentation. The target features a motif of three equally-spaced rectangles which is patterned many times in continually decreasing sizes. The particular target used in this manuscript consisted of a 10 μm thick layer of SU-8 polymer (which has a distinctive IR absorption spectrum) on a barium fluoride disk (which is transparent to mid-infrared light). In all examples, we examined one region of the target: cycle 3, elements 5 and 6, which contain 'bars' of widths of approximately 35 and 39 μm, respectively. This particular structure was chosen because it approaches the size limit for targets which are well-resolved by commercial FT-IR imaging instruments.

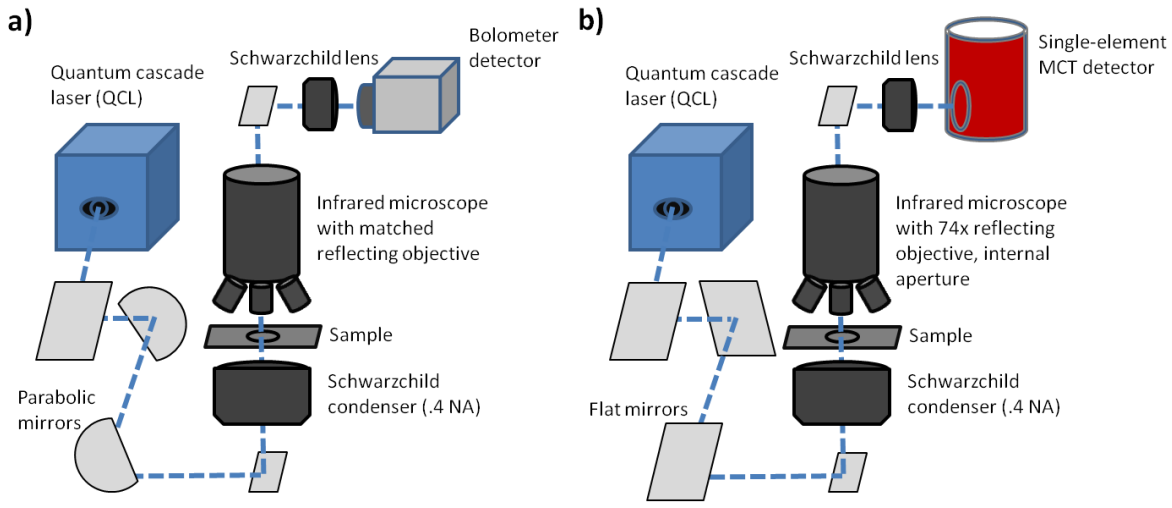

Figure 2.1. Schematics of the two DF-IR systems evaluated in these experiments. Both utilize a tunable, narrow-bandwidth mid-infrared QCL and the same infrared microscope frame. A) QCL coupled to an uncooled bolometer camera. A parabolic mirror pair is used for 10:1 beam expansion before the microscope. B) A cooled single-element MCT detector is utilized with an adjustable aperture that focuses at the sample plane for point measurements. Flat mirrors replace the parabolic mirror pair so that the beam is not expanded.

We first acquired images of the standard USAF sample using a bolometer array detector, shown in Figure 2.2a. Uncooled detectors have also been proposed for use in IR spectroscopic imaging measurements but

coupling a bolometer to a globar source produced exceptionally low quality data.[29] The higher flux of the QCL makes imaging with a microbolometer feasible. The lower cost of the microbolometer as well as its larger format compared to the majority of available cooled array detectors makes this a very attractive technology. With a more even illumination, such an imaging system could compete against the established FT-IR imaging systems that usually employ a thermal source (globar) and a cooled array detector. The data acquired using a QCL were compared to those acquired from a commercial FT-IR imaging spectrometer in Figure 2.2c. It is notable that the QCL-based system used a low-performance bolometer while the FT-IR imaging system is the best available today[30] in terms of signal to noise ratio (SNR). The data demonstrates that the coupling of a QCL to an imaging system can be achieved and presents an opportunity to compare with FT-IR imaging systems even though the two sources are significantly different in nature.

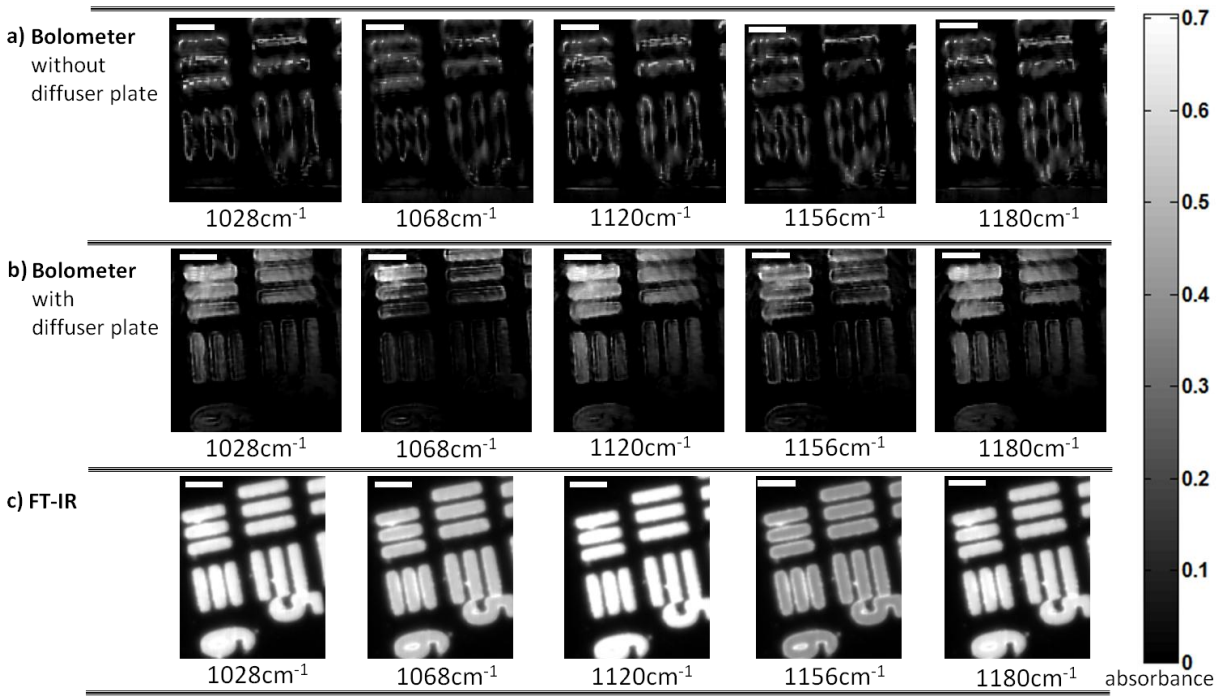

Figure 2.2. USAF 1951 optical resolution target absorption images (cycle 3, elements 5 and 6) as acquired by three different instruments. A) QCL+bolometer system without diffuser plate. B) QCL+bolometer system with rotating diffuser plate. C) commercial FT-IR instrument. Scale bar = 100 μm.

A fine structure overlain with the target was apparent in the QCL-based data and was the most striking difference from commercial imaging. We hypothesized that this effect arose from multiple reflections and scattering from the sample as well as etaloning at the detector, both of which were exacerbated by the spatial coherence of the laser. To remedy this, we placed a diffusing element in the beam path. With the use of this diffuser (Figure 2.2b), the fringes and interference were not entirely eliminated but image quality was substantially improved. Such a diffuser has been used in at least one other study[31] but its effect was not presented and the effects of laser coherence on images were not shown. The diffuser employed was a transparent salt plate that was heavily scratched on one face to induce random phase shifts in the beam. Simply placing the plate in the path of the beam had little effect as a structured spatial correlation in the beam was still transmitted (images not shown). As a result, the diffuser plate was

rotated. Rotating the plate allows energy to be more evenly distributed over the specimen but multiple images must be acquired during the rotation. Images acquired by the QCL+bolometer instrument with the diffuser plate can be seen in Figure 2.2b. Compared to Figure 2.2a, the fine structure is markedly reduced. A slight shadowing effect can be seen in both sets of images, likely the result of an imperfectly aligned system. Even with rotation, the collected image is a function of the exact rotational position of the plate at the time of acquisition. Scratching the plate can never yield completely randomized scattered light; regions of pronounced scratches or less scratching retain some coherence and are projected through the sample and onto the bolometer. A series of 64 sequential images was captured and averaged to 'smooth out' this enduring structure. As it is not a perfect solution, the 'swirling' pattern caused by the rotating diffuser plate is evident in the images, but this degrades the images far less than without the diffuser in place. In addition to reducing the coherence of light, the scratched diffuser plate also causes additional scattering. This is ordinarily undesirable, as light scattered (or absorbed) by the plate cannot be used for imaging, but in this setup the losses were small compared to the available flux.

The effects of the beam's spatial coherence are clearly an issue of concern if QCLs are to be used for IR imaging. A theoretical framework to explain image formation while including the light coherence is desirable. The emission from a coherent laser source implies that photons in different spatial locations are in phase with one another. The electric field associated with light scattered at any point from the sample can interfere with light transmitted from other points. The amplitude of the electric fields are added and quadratically encoded in the resulting intensity, which is measured by the detector. As opposed to a QCL, the globar commonly used for FT-IR spectroscopic imaging is an incoherent source; as a result, scattered and transmitted intensities are added. Optical effects encoded in the image in this case are significantly muted, as can be seen from an apparently high absorbance at the edges of the bars (e.g., especially pronounced at 1156 cm^{-1}) due to the refractive index mismatch. A complete description of the recorded absorbance is possible using recently developed electromagnetic theory-based models of image formation in IR microscopes and specific sample shapes.[32,33,34] A more recent formulation may be

especially useful for examining the effects on recorded data of periodic structures in samples.[35] At this time, the expectation that the coupling of QCLs to existing microscopy systems will yield an equivalent system with higher SNR is unfounded. Significant advances in understanding the resulting data and its spatial-spectral relationships would be required before optimized QCL-based instruments can be designed and successfully implemented.

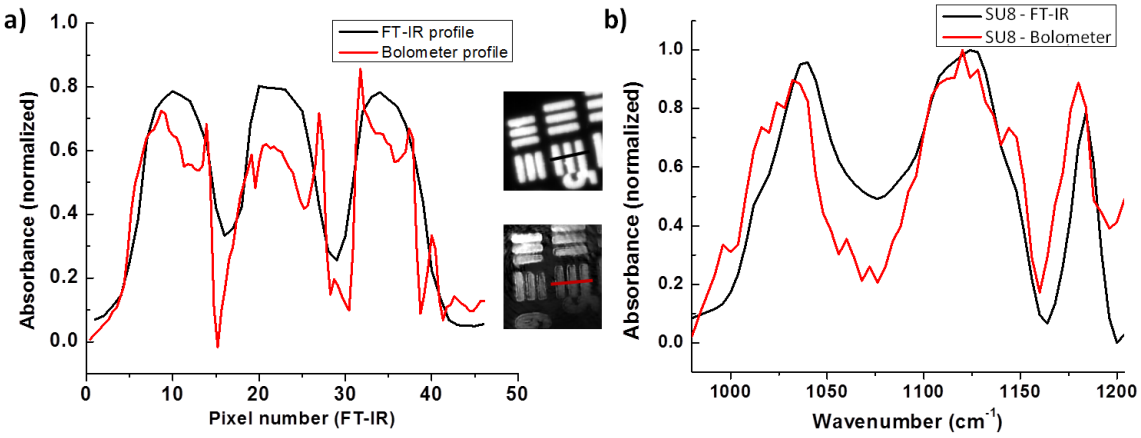

Figure 2.3. (A) Bar-target motif profile for the commercial FT-IR instrument and the QCL+bolometer system. Because the two detectors contain a different number of pixels, the scale of the measured bolometer profile was adjusted to match that of the commercial instrument. (B) Absorbance spectra of SU-8 polymer for both the commercial FT-IR system and the QCL+bolometer system. The commercial system recovers the absorbance spectrum using an inverse Fourier transform, while discrete absorbance measurements were taken every 4cm^{-1} for the bolometer system.

In comparing bolometer measurements to those acquired by a commercial FT-IR system, "image quality" can be described by several different factors, including spatial resolution, spectral quality, and signal-to-noise ratio. Spatial resolution is approximately equal for the two systems, as seen by the measured profiles. Figure 2.3a shows the bar motif profiles for target 5, cycle 2 for both the commercial FT-IR instrument and the bolometer plus diffuser plate setup. After a correction for pixel size (the size per pixel in the FT-IR images is almost 2.5 times as large as those in the bolometer images), it is apparent that the

two are on the same order. In fact, because there are more pixels representing the same area for the bolometer images, this system has the potential to achieve the higher quality of images. The relative equivalence of images is not surprising as the optical setup is similar; however, the relative equivalence in the presence of coherence effects is encouraging. This may indicate that QCL based systems could be effective for qualitative imaging and will reasonably correlate with FT-IR imaging data, provided that absorbance is high and scattering is not especially strong. For weak absorbance and domain sizes on the order of the wavelength, results between the two would deviate significantly.

Arguably more important than resolution in chemical imaging is the quality of the spectra generated. When sequential images across a range of evenly-spaced wavelengths are acquired, an absorbance spectrum at each point is generated. Figure 2.3b shows the spectrum of SU-8 as acquired by the bolometer instrument with diffuser plate and as acquired by the commercial FT-IR system. It is clear from the similarity of the band shapes that the bolometer instrument is capable of collecting a representative spectrum. The comparable widths of the bands justify that the tunable QCL beam has a sufficiently narrow spectral width to probe these absorbance bands. While the band intensities are not identical to those determined by the commercial instrument, this is to be expected. Bolometers are inherently noisier than cooled focal plane arrays and are generally not considered of being capable of quantitative measurements. The differences may also be due to optical effects, as reported previously for other configurations,[32,33,34] but need to be examined in detail using available theory and simulations. The signal-to-noise ratio (SNR) of acquired data is another important aspect of image quality which should be evaluated. Due to uneven illumination in this setup, we have measured the signal-to-noise ratio as varying from less than 1 to as large as 32. These values are for images whose acquisition time is on the order of milliseconds and signal averaging may well improve the SNR if the noise is detector dominated. It can be argued that the QCL system has a higher capacity for signal-to-noise ratio than does the FT-IR instrument: not only is the source power much higher at each individual wavelength measured (between 200mW and 400mW at most wavelengths), but the entire dynamic range of the detector is used for a

single wavelength at a time rather than evaluating all wavelengths simultaneously. A detailed discussion of the merits of DF-IR systems relative to FT-IR imaging systems on this issue is available.[36]

In comparing the results of the QCL plus bolometer system to those given by the commercial FT-IR system, it is clear that on most accounts FT-IR outperforms the bolometer. There is much room for improvement in the bolometer system, including the development of a more effective method for homogenizing the QCL beam and breaking up beam coherence without introducing additional artifacts. Even without these improvements in place, the QCL plus bolometer system may be able to offer unique advantages over FT-IR methods in certain applications. The higher flux makes measurement in aqueous environments possible.[37] It has been recently demonstrated that only a handful of bands are required for certain biological analyses,[7] making acquisition of the entire spectrum redundant. Discrete frequency methods could offer a distinct speed advantage in cases where only some bands are required for measurement. Additionally, due to the direct acquisition of transmission data without the need for performing an inverse Fourier transform, the possibility for real-time infrared microscopy and monitoring becomes available.

Given the multichannel detection advantage and the emergence of IR imaging systems with exceptional quality,[10,38] we focused on widefield microscopy applications of the QCL source. Interferometric instrumentation is not appropriate for point mapping applications due to the very low throughput of a broadband source through a small aperture. Discrete frequency imaging using a focused, filtered broadband source also has too low a throughput for such uses. One of the strongest arguments for the use of a QCL as an infrared spectroscopy source is the high power at discrete frequencies and focusing ability for high-throughput point mapping measurements. The large flux, focused into a single channel, may offset some of the speed advantages of multichannel detection and the need to diffuse the beam over a large area. The use of point illumination may also be used to circumvent the fine structure seen in images as there would not be a scattered and transmitted wave at two different points to interfere. As a final instrumentation setup, we examined the use of QCL for point mapping.[9]

For point mapping, the expansion optics (gold-coated parabolic mirrors, iris) and diffuser plate were removed from the DF-IR setup. This kept the unaltered beam tightly focused (less than 2mm diameter) upon entering the microscope. The bolometer camera was replaced with a cooled single-element MCT detector, allowing for enhanced sensitivity and signal-to-noise. For simple point measurement rastering of large areas, a QCL system will not be able to best an FT-IR microscopy system with a globar source. The speed of these conventional widefield systems would far outperform QCL point mapping. The advantage of a QCL source lies in the ability to create truly diffraction limited spot sizes by using large NA objectives and small apertures. We replaced our objective with a 74x reflecting objective of 0.65 NA. The high magnification of the objective meant that the microscope's built-in adjustable square aperture could be used to create a very small effective aperture (0.72 μm) for point-imaging. This aperture size is significantly smaller than the range of illumination wavelengths for imaging and smaller than any objective reported for a globar or synchrotron-based system.[39,40,41] Even with this small aperture in place, a large SNR was observed, and by rastering the stage in increments 1μm or 0.5 μm, spectral data were obtained over larger areas. To date, this is the smallest far-field aperture and smallest point spacing reported. While we caution that diffraction still limits the spot size, the improvement over ~10 μm apertures is obvious in the recorded data. Figure 2.4 demonstrates data acquired from two polystyrene spheres that are approximately 10 μm in diameter. The entire image would consist of significantly fewer pixels with a globar point mapping system or a synchrotron system which provided any appreciable SNR. The pixel density is over 100 times that of a synchrotron and nearly 1000 times more than that of a globar.[38] In this manner, QCL-based point mapping systems present a new opportunity to image small regions and generate images that are of high pixel density for small feature recognition. The reproduction of structure is quite faithful. At ~10 μm imaging wavelength, the 10 μm diameter spheres can be clearly seen and easily separated.

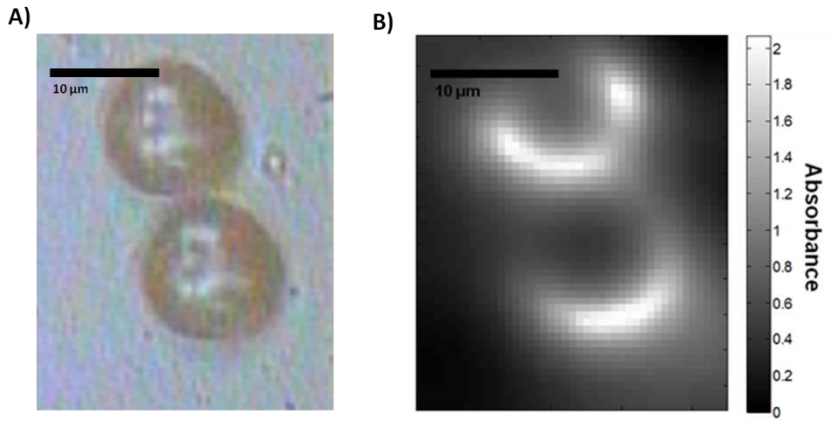

Figure 2.4. A) White-light image of two touching polystyrene spheres, diameter 10µm. B) Point-mapping IR absorption image of the same two spheres at 1080cm^{-1}, 0.5µm steps, 0.72µm aperture.

This point mapping method also allows for the investigation of infrared scattering effects with enhanced clarity. Scattering by the edges of structural features in infrared imaging is extensive, but difficult to quantify in a widefield regime. The corner of one of the 'bars' in the USAF 1951 optical resolution target from the first set of experiments was imaged with both a commercial FT-IR instrument and the point mapping setup at 1080 cm^{-1} to compare the clarity of scattering effects. As imaged by the commercial system in Figure 2.5a, the feature shows an increased loss of transmission at the edges (misinterpreted by the instrument as increased absorbance). The image shows no well-defined structure to the increased scattering. This is evidenced by Figure 2.5b which shows an absorbance profile of one row of pixels in the image. When imaged by the point-mapping system in 0.5um steps, it becomes apparent that there is a well-defined structure to the scattering that was not discernible in the commercial image. Figure 2.5c shows the multiple spatial maxima and minima that occur with edge scattering, and Figure 2.5d shows one row of pixels in greater detail.

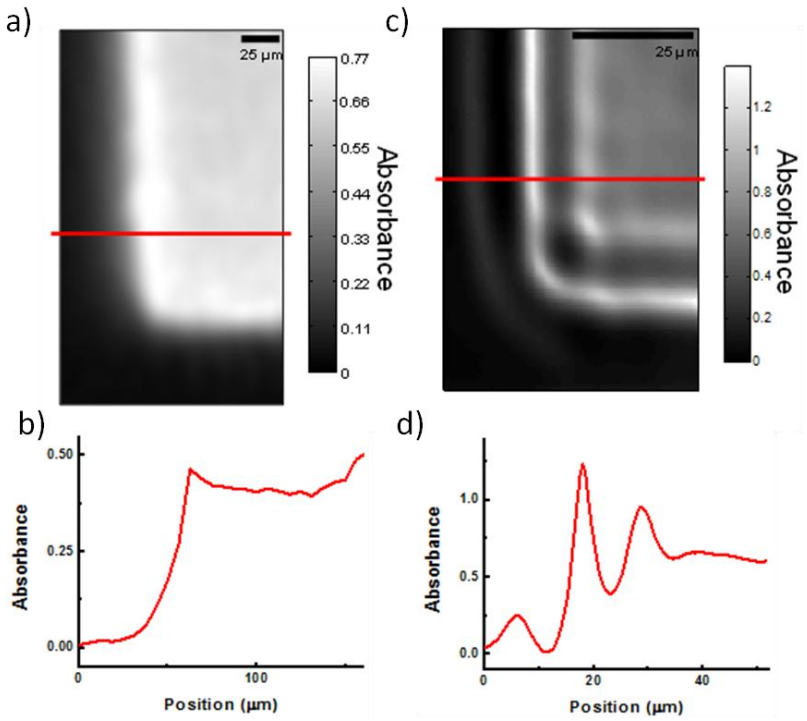

Figure 2.5. A) Image of a USAF 1951 bar target corner with a commercial FT-IR instrument at 1080 cm^{-1}. The increased 'absorbance' at the sharp feature edges is actually due to increased scattering. B) Graphical profile of one row of pixels from 2.5a. Aside from some blurring, there does not appear to be well-defined interference pattern at the feature edges due to scattering. C) Image of the corner with the point-mapping instrument and a 0.72 µm aperture at 1080 cm^{-1}. The edge structure looks starkly different from that of 2.5a. D) Graphical profile of one row of pixels from 2.5c. Each edge shows a series of minima and maxima that were not discernible with a commercial FT-IR instrument.

Section 2.4 Conclusions

The latest developments in tunable QCL technology have allowed for lasers with large tuning ranges, narrow spectral linewidths and high fluxes to the point where these become feasible sources for discrete-frequency infrared imaging. We have demonstrated an application of a QCL for use as a source in infrared microscopy. When coherence is reduced and the beam is expanded, images of an optical resolution target can be acquired on a bolometer-type camera. These images are comparable to commercial FT-IR measurements in spatial resolution, but lack in spectral clarity and signal-to-noise ratio. When used for point-mapping, the QCL provides a throughput advantage unmatched by incoherent

broadband sources and allows for high-resolution infrared imaging through a small aperture. These properties of QCLs as an infrared source allow for additional advantages, including rapid widefield imaging at single wavelengths and the possibility for real-time infrared monitoring.

CHAPTER 3: TRANSMISSION RAMAN TOMOGRAPHY ON A CYLINDRICAL TISSUE PHANTOM

Section 3.1 Introduction

Biological samples are optically turbid in the near infrared (NIR) spectral region, leading to diffusion of light[42] throughout the sample upon illumination. Diffuse optical tomography (DOT) techniques can be used to record absorption and scattering properties[43] wherein quantifying the diffuse propagation of photons through translucent structures is an active area of research.[44,45] While understanding light propagation given the structure of the sample can be considered the "forward" problem, the recorded data between multiple NIR sources and detectors can be modeled to and recover local light attenuation (solving the "inverse problem").[46,47,48] Both problems are critical to developing new measurement applications, for example, human breast imaging for tumor detection[49,50,51] and functional brain imaging in both humans and small animals.[2,52,53] Several distinct implementations of NIR DOT exist to acquire information from turbid samples, many of which incorporate additional features that are complementary to attenuation measurements.[54] For example, using pulsed excitation or frequency modulated CW sources allows for phase delay measurements leading to a greater ability to determine scattering properties at the mm-length scale[55,56,57] The use of spatial priors, such as tomographic images from x-ray computed tomography (CT) or magnetic resonance imaging (MRI), can also lead to models with enhanced spatial resolution.[8,58] Multiple illumination wavelengths[13,59] can be used to quantify the spatial distribution of oxygenated and deoxygenated hemoglobin, water and lipid content in tissues, or the concentration of an exogenous contrast agent.[9,10,11,60,61] While these technological achievements have demonstrated excellent capability and progress, NIR spectroscopic measurements are inherently limited in chemical specificity. The intrinsic NIR spectral absorbance signal arises from broad vibrational overtones as opposed to fundamental vibrational modes that are specific to molecular functional groups.[62] Thus, as with many

forms of tomography, information related to chemical specificity is limited or is determined by the use of exogenous contrast agents. One avenue to overcome these limitations is to incorporate vibrational spectroscopy into tomographic techniques to probe fundamental vibrational modes, providing detailed molecular information without the need for exogenous contrast agents in thick samples.

Raman spectroscopic instrumentation and data analysis methodology for probing diffusive media have improved in efficiency and prediction capabilities in recent years. For example, spatially-offset Raman spectroscopy (SORS) has enabled spectral data acquisition from objects buried several millimeters deep within turbulent samples, including both non-biological polymers[63,64,65] and tissue analyzed in vivo.[66] The recovery of subsurface spatial information has also been demonstrated using the SORS approach.[67,68] With the use of spatial priors and a backscattering probe, spectra from targets buried within translucent media have been localized to within a millimeter.[69] Raman spectroscopic measurements in a transmission geometry have also been performed on tissues with spatial priors, showing good localization of the detected spectral signal.[70] Despite these advances, a generalized Raman tomography method analogous to DOT has not been demonstrated. We hypothesize that Stokes-shifted photons generated from Raman scattering during a DOT experiment can be used to determine the chemical identity of buried analytes. Here, we report a method for using Raman-scattered photons to gain vibrational molecular information from a sample in a simple DOT-like configuration. Using a series of tissue phantoms, we investigate the Raman response of embedded Teflon (PTFE) spheres as a function of phantom rotation and the illumination-detector geometry. Both single point and multiple point detectors in three configurations that span a range of practical geometric implementations are considered. To determine the performance limits of this approach, we evaluate light fluence and sampling power using two distinct modeling methods: diffusion-regime radiative transport calculation and non-diffusion Monte Carlo simulation. Together, the experimental and theoretical approaches seek to determine whether transmission Raman tomography measurements can provide information similar to their DOT counterparts with the additional benefit of detailed molecular specificity.

Section 3.2 Instrumentation and Methods

Phantom Specimens and Fabrication

Tissue phantoms were fabricated by dissolving 1 gram of agar (Sigma-Aldrich) in 50 ml of water at 95°C. Different volumes of 20% Intralipid (Sigma), an oil emulsion that is commonly used to mimic the scattering properties of fatty tissue,[71,72,73] were added to increase the scattering potential. 0.25ml or 1.25ml per 50ml of water was added to produce phantoms with a total Intralipid concentration of 0.1% or 0.5% by volume. A 0.1% concentration of Intralipid represents the lower limit of what is opaque to the naked eye, while a 0.5% solution close to the scattering level exhibited by epithelial tissue.[74,75,76] The solution was poured into the wells of a cell culture plate. One PTFE sphere of 1/8" diameter or two spheres of 1/16" diameter were suspended in each well by thin histology needles, and the plate was allowed to cool in a refrigerator for approximately one hour. The resulting phantoms were cylindrical, 1 cm in diameter and approximately 2 cm tall. Each sphere was positioned such that its middle sat approximately 1.2 cm above the base of the phantom. The radial position of the spheres, as well as the distance between two spheres embedded in the same phantom, were experiment-dependent.

Raman Instrumentation

The instrument comprised of a 785 nm excitation laser and CCD-coupled spectrometer with a pre-stage notch filter (785nm RXN1, Kaiser Optical Systems, Ann Arbor, MI), a fiber-optic bundle detector and a motorized rotation stage, as shown in Figure 3.1. In all cases, the laser and detector were held at a constant height at the level of the PTFE sphere or spheres while the cylindrical phantom was rotated about its vertical (circularly symmetrical) axis. This allowed for a single source/detector combination to sample the phantom from multiple angles, a requirement of optical tomography. [21]

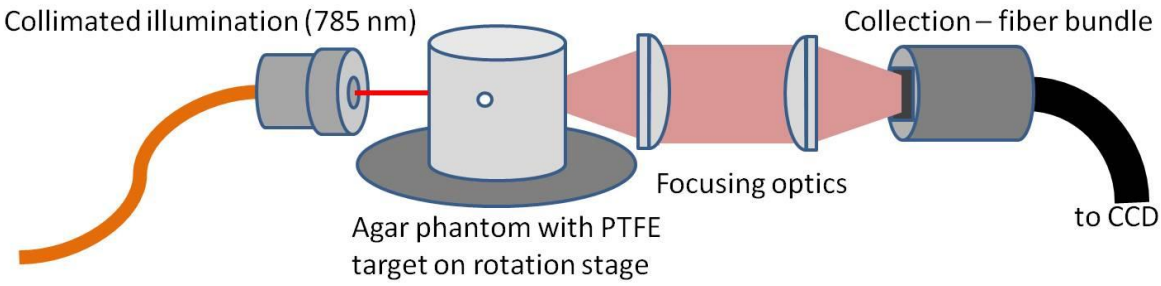

Figure 3.1. Instrumentation for Raman tomography experiments consists of a collimated illumination source, a rotation stage that holds the phantom, and a fiber bundle serving as a detector. Two achromatic doublets couple light exiting the phantom into the fiber bundle. Both the illumination and collection fibers are centered on the phantom at the height of the PTFE sphere(s).

The 400mW CW laser at 785nm (Invictus, Kaiser) was fiber-launched and passed through a collimator to produce a 1.25 mm diameter beam. Collection was performed via two achromatic doublets which focused the photons exiting from the phantom onto a 50-fiber bundle (100 um diameter each, in an approximately 5x10 array) (Fibertech Optica, Kitchener, Ontario, Canada). The focal lengths of these achromats were 60mm (focusing) and either 75mm or 200mm (collection). The output of the fiber bundle was imaged onto a spectral CCD (iDUS, Andor Technology, Belfast, Northern Ireland). The motorized rotation stage (NR360S, ThorLabs, Newton, New Jersey), controlled by LabView (National Instruments, Austin, Texas), was stepped clockwise in 4.5 degree increments in all experiments for a total of 80 discrete sampling angles.

Experiments

For phantoms containing a single sphere, three separate instrumentation configurations (as shown in Figure 3.2) were considered. In the first, shown in Figure 3.2a, the source and detector were kept at a 180^{o} angle while the phantom was rotated through 80 positions to demonstrate the insufficiency of using a single source-detector angle. Acquisition time was three minutes per step (two frames of 90 seconds each to aid in data processing). The second experiment involved varying the angle between the source and

detector, shown in Figure 3.2b. In addition to 180^{o}, the source was moved relative to the detector to form angles of 135^{o}, 90^{o}, and 45^{o}. This setup mimics the "circular fan-beam" geometry which is commonly used in diffuse optical tomography experiments.[7] For each source position, the stage was rotated through the full 80 steps and two spectra of 30 seconds each (as opposed to 90 seconds) were acquired at each step. In the final configuration, the source/detector angle was returned to 180^{o}, but the achromatic collection lens nearest to the phantom was replaced with one of focal length 200mm as shown in Figure 3.2c. The entire detector setup was moved an appropriate distance away from the phantom to keep the fibers in focus. This expanded the collection region from an area of approximately 0.97 mm x 1.3 mm to 2.9 mm x 3.8 mm with the intent of being able to collect spatial information from each individual fiber. This fan-like geometry was chosen to mimic the cone-beam transmission computed tomography (CT) source-detector configuration.[77]

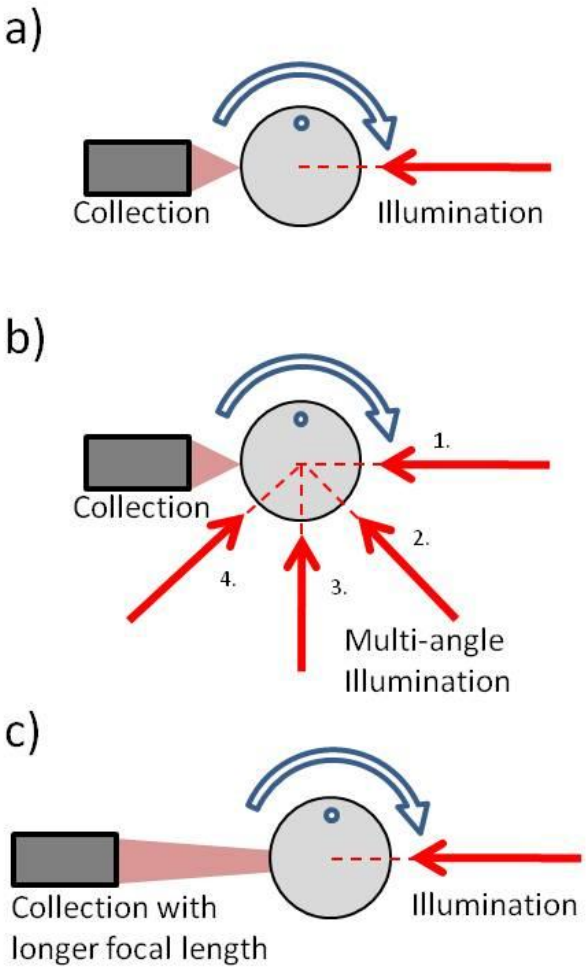

Figure 3.2. Three instrumentation configurations corresponding to the three experiments performed. A) Illumination and collection are fixed at a 180 degree angle. Measurements are taken as the phantom is rotated in 80 steps of 4.5^{o} each. The fiber bundle is treated as a point detector for 80 total measurements. B) Multiple scans are taken with the source forming four positions with the detector (180^{o}, 135 ^{o}, 90 ^{o} and 45^{o}). The total number of measurements taken is 320 (4 x 80). C) Illumination and collection are fixed at a 180^{o} angle as in setup a), but the focal length of the collection has been increased from 75 mm to 200 mm. As a result, the total area of collection is larger and the fiber bundle can no longer be treated as a point detector – the signals from (ten) individual fibers were evaluated for 800 total data points.

A series of experiments involving phantoms with two PTFE spheres were also performed. Using the instrument setup with the longer focal length collection (experiment ‘c’ above) and an additional 30 mm focal length lens to focus the collimated illumination beam in an approximation of a point source (see

later discussion), the response from two spheres was investigated. Additionally, a third series of experiments in which the Intralipid content of the two-sphere phantoms was increased to 0.5%, was performed in the same manner with two spheres and a longer focal length. The quality of the reconstructions was evaluated by comparison to micro-CT images showing absolute sphere positions.

Data Processing

All data processing was done in Matlab R2009b (The MathWorks, Nantucket MA). A median filter was applied to all collected data to correct for the cosmic ray 'spikes' which appear on the CCD. The two Raman bands of interest are PTFE (732 cm^{-1}) and Intralipid (~800-820 cm^{-1}). A multilinear "rubber band" baselining procedure was used to remove the background, and the area under each band was calculated. During reconstructions, both the absolute intensity of the PTFE signal and that of the Intralipid signal are utilized. The intensity of the Intralipid band is directly proportional to the number of photons reaching the detector for that measurement, and can be considered an internal standard which accounts for any discrepancies in the distance between source and detector or in the amount of light collected. In high-scattering samples where the Intralipid band is obscured by noise, the band's value is approximated as being proportional to the average intensity of the entire CCD chip.

Computerized Tomography Reconstruction

Nirfast [developed by the Pogue group at Dartmouth University, www.dartmouth.edu/~nir/nirfast], is an open-source software package for simulation of DOT experiments and for DOT reconstructions from real or simulated data.[78] Based on a finite-element method for calculating photon fluence though specified geometries, the two processes that can be modeled (NIR absorbance and fluorescence emission) can be seen as analogous to Raman scattering events (conversion of Rayleigh scattered to Stokes scattered light). While the physical processes behind these two are not the same, they are similar enough to warrant the use of Nirfast as a first approximation for 2D reconstructions from experimental Raman data. For reconstructing experimental data, a circular finite element mesh was generated within the program.

Source and detector locations were added to match each experimental setup, and the experimental data were ordered and normalized to match the range of the signal from a forward simulation of a 'blank' mesh with no absorbing target.

Also evaluated was a Monte Carlo simulation written in-house for modeling photon fluence. Using a 2D pixel mesh, the reconstruction mathematics and assumptions conserved between the two methods. Although more computationally intensive, Monte Carlo simulations allow the user to overcome certain assumptions made by the radiative transport equation (including the use of a non-idealized point source, implementation of geometrically-accurate detectors, and photon migration that does not follow the diffusion regime) which may not be appropriate for certain Raman experiments. Monte Carlo studies which simulate the generation and propagation of Raman photons through turbid media have been performed recently.[79] In a similar manner, we compare the results of Monte Carlo simulations to those of Nirfast to show that the physical processes that govern Raman tomography experiments differ significantly from DOT experiments and that these two modalities need to be treated as separate entities.

Section 3.3 Results and Discussion

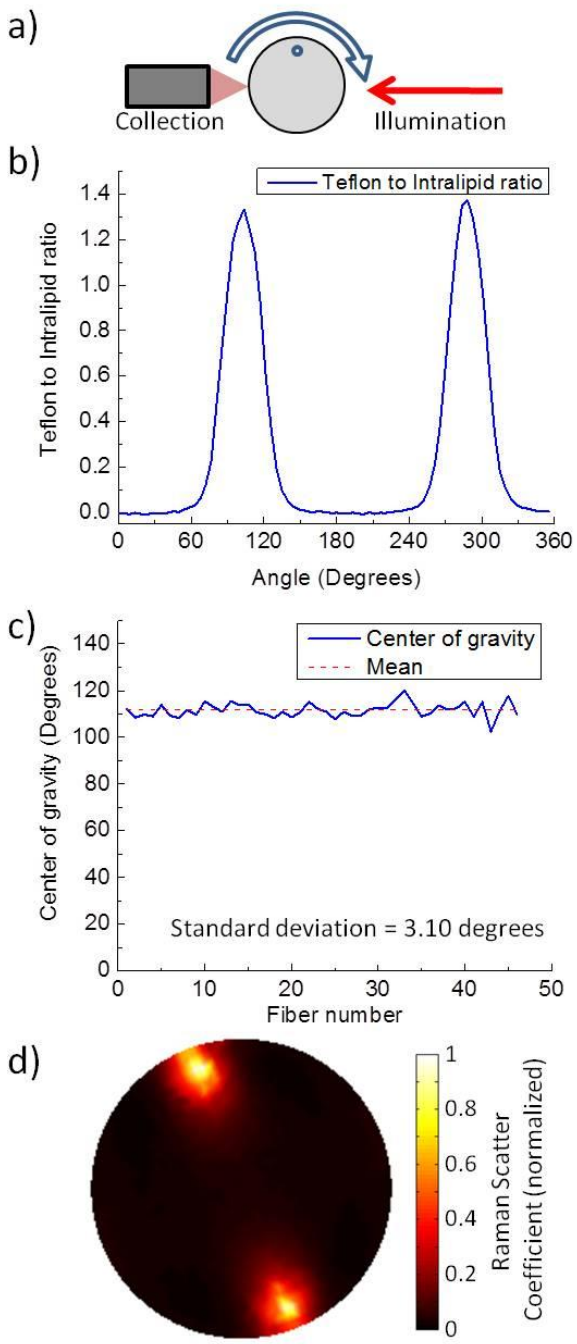

Figure 3.3. A) Schematic for the 180° setup, including the direction of rotation and the approximate starting position of the PTFE target relative to the source and detector. B) PTFE to Intralipid Raman photon ratio as a function of phantom rotation, average of all fibers. C) Center of gravity measurements for each fiber-optic in the detector bundle. D) Reconstruction from Nirfast.

We first evaluate the radiative transport model (Nirfast) for reconstruction. Figure 3.3a illustrates the simplest configuration and the recorded Raman signal of a PTFE sphere relative to Intralipid as a function of rotation (Figure 3.3b). Two maxima are observed: one when the target passes the source and another when the target passes the detector. These two maxima are spaced by approximately 180^{o}, which is explained by uniform rotation of the target through 360^{o}. In-between the two maxima, no Raman signal is observed; the collected photon count at these points is below the spectrograph's limit of detection.

Each of the 50 fibers from the detector is mapped onto a different region of the CCD camera, and the response from each fiber can be individually determined. The behavior of individual fibers (detectors) set along the waist of the phantom would be similar to the results seen in Figure 3.3b: the PTFE sphere will pass by each fiber and the source during rotation, resulting in two maxima with slight position shifts as a result of fiber position. If the fibers are all packed closely together, this difference is expected to be minimal; if the fibers are spaced at larger intervals, this difference will be much more pronounced. Figure 3.3c plots each fiber's (48 total) center of gravity for the second maximum (corresponding to when the sphere is closest to the detector) as a function of phantom rotation. The fibers show a standard deviation of 3.1 ^{o}, indicating that the majority of the fibers 'see' the sphere pass by within six degrees of rotation. This small variation is to be expected because the assembly's collection area spans one square millimeter, contributing a very small angular response of less than three degrees. The two maxima (target near source and target near detector) are similar in height, width, and shape. Without angular information it is not obvious how to distinguish one from the other. Performing a 2D reconstruction on the data with Nirfast, as shown in Figure 3.3d, confirms this observation: the program predicts two targets separated by 180 degrees. This result reinforces the well-proven notion that multiple collection angles are needed to accurately determine the position of targets buried in scattering analyte.[7]

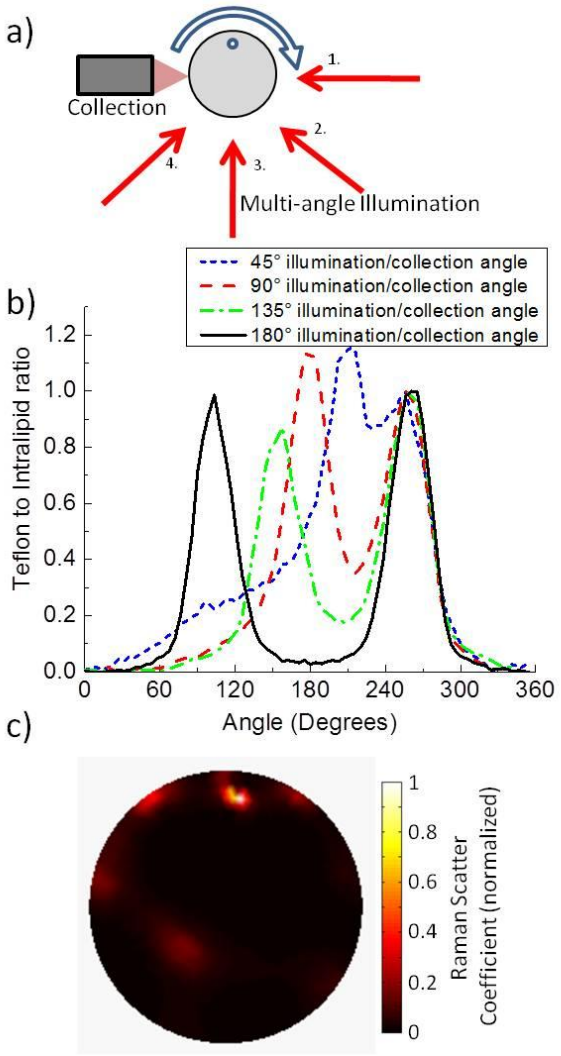

Figure 3.4. A) Schematic for the multi-angle setup, including the direction of rotation and the approximate starting position of the PTFE target relative to the sources and detector. B) PTFE to Intralipid Raman photon ratio as a function of both phantom rotation and source/detector angle. C) Reconstruction from Nirfast.

Figure 3.4b displays Raman signal versus rotation angle for multiple source locations ("circular fan-beam" geometry). The data have been normalized to the second maximum. As in the previous example, each full rotation shows two maxima corresponding to when the target passes the source and the detector. The maxima show an amount of separation roughly equivalent to the corresponding source-detector angle. Maxima corresponding to the sphere passing the detector do not change in position. The Nirfast

reconstruction in Figure 3.4c supports the observation that multiple illumination/collection angles gives greater insight as to the location of the target.

Although one target is predicted, 'shadowing' occurs in regions not occupied by the sphere. The primary cause of this stems from a discrepancy between how illumination is modeled and how the phantom is actually illuminated by our instrument. The radiative transport equation is forced to assume a perfect point source for illumination – for measurements over long distances, samples with high scattering coefficients, and fiber-launched illumination in contact with the sample, the effective angle of illumination is very large. During photon travel from source to detector, many scattering events will occur, making a point-source illumination approximation very appropriate. In this experiment, a collimated beam is used as the source, meaning that the illumination is highly directionalized within the sample. The difference between these two models is illustrated in Figure 3.5a, which compares the photon fluence at four points on a homogeneous phantom as simulated in Nirfast and measured using the experimental setup. It is immediately apparent that these two models are not equivalent. With a point source illumination, photon density at any position in the phantom is directly proportional to the distance from the source. Collection at 45^{o} relative to the source is more intense than 90^{o}, etc. In the experimental setup, fluence is greatest at a collection point 180^{o} relative to the source, which is the exact opposite of the simulation. In this particular experimental setup, the source directionality, scattering level, and measurement distance are such that the assumption of photon diffusion behavior does not hold. While the fluence in regions between the source and detectors at angles smaller than 180 is highly dependent on the choice of model, the fluence at detector positions with angles very close to 180 are very similar to one another in both models. As such, it can be argued that, for detector positions close to and centered around 180 relative to the source, a point source approximation may be suitable for the experimental setup's collimated beam illumination.

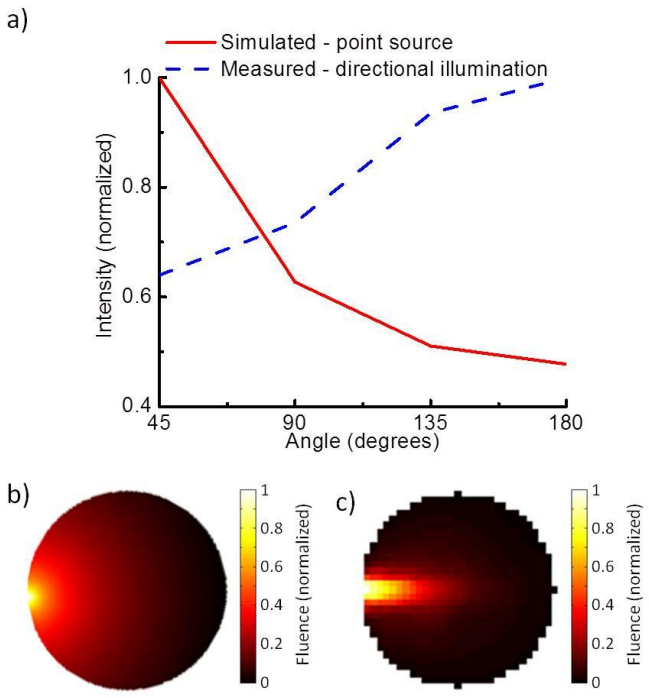

Figure 3.5. A) Illumination fluence at the phantom border at four different angles relative to the point of illumination. Solid line: calculated fluence from the radiative transport equation. Dashed line: measured fluence using a tissue phantom (0.1% Intralipid, no targets). B) Illumination structure for an idealized point source. C) Ray tracing simulation showing the illumination structure for a directionalized laser source.

In order to collect at a number of angles near 180° from the source, the fiber pattern was focused with a lens of length 200 mm, significantly increasing the size of the fiber pattern as projected onto the phantom (as illustrated in Figure 3.6a) to nearly 4 mm across. In this manner, the angles formed between the source and detectors ranged from 0-10.4 degrees. Upon measuring the phantom with this setup and summing the responses of all 48 active fibers, the resulting response shown in Figure 3.6b is significantly different from that in Figure 3.3a. While two peaks separated by approximately 180° are observed, one peak (corresponding to the target passing the detector array) is significantly shorter and wider, resulting from the increased spacing of the detectors. This reasoning is confirmed in Figure 3.6c, in which the standard deviation of the peak position for all fibers is increased to 23.9. The wider spacing of the fibers

implies that more angular information is collected. Upon performing a Nirfast reconstruction using 10 individual fibers spaced across the width of the fiber pattern (and, as a result, tenfold the number of data points as compared to a single detector at 180° from the source), the image in Figure 3.6d is generated. A single target is predicted with minimal 'shadowing' artifacts seen from collecting at angles smaller than 180° from the source, indicating that errors resulting from an incorrectly predicted illumination structure are reduced when source-detector angles are large and span a small range.

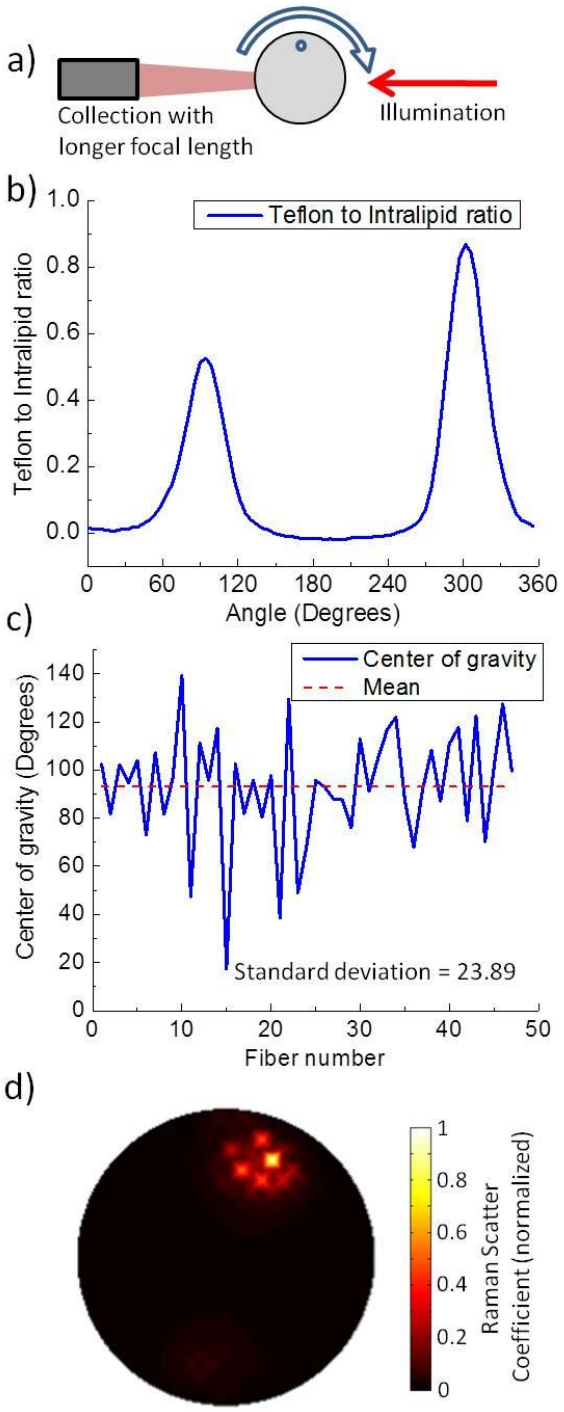

Figure 3.6. A) Schematic indicating a longer detector focal length and, in turn, a larger collection area by the detector. B) PTFE to Intralipid Raman signal ratio averaged over all fibers. C) Fiber optic center of gravity of all collection fibers. D) Nirfast reconstruction using 10 individual fibers spanning the length of the fiber pattern per rotation angle.

While it has been demonstrated that the correct number of targets (and an approximation of target position) can be recovered using this large fiber pattern setup, the validity of this technique cannot be determined unless a) the separation of two closely-spaced targets and b) the accurate determination of the positions of these targets can be demonstrated. In order to do this, three changes were made to the experiment summarized in Figures 3.2c and 3.6a: two 1/16" diameter spheres (instead of one 1/8" diameter sphere) were embedded in the phantom with close spacing (roughly equal to one sphere diameter), 'fluorescence' Nirfast reconstructions were used (as to separate PTFE and Intralipid responses and normalize each to a simulated blank), and micro-CT was performed on each phantom in order to determine the exact target positions.

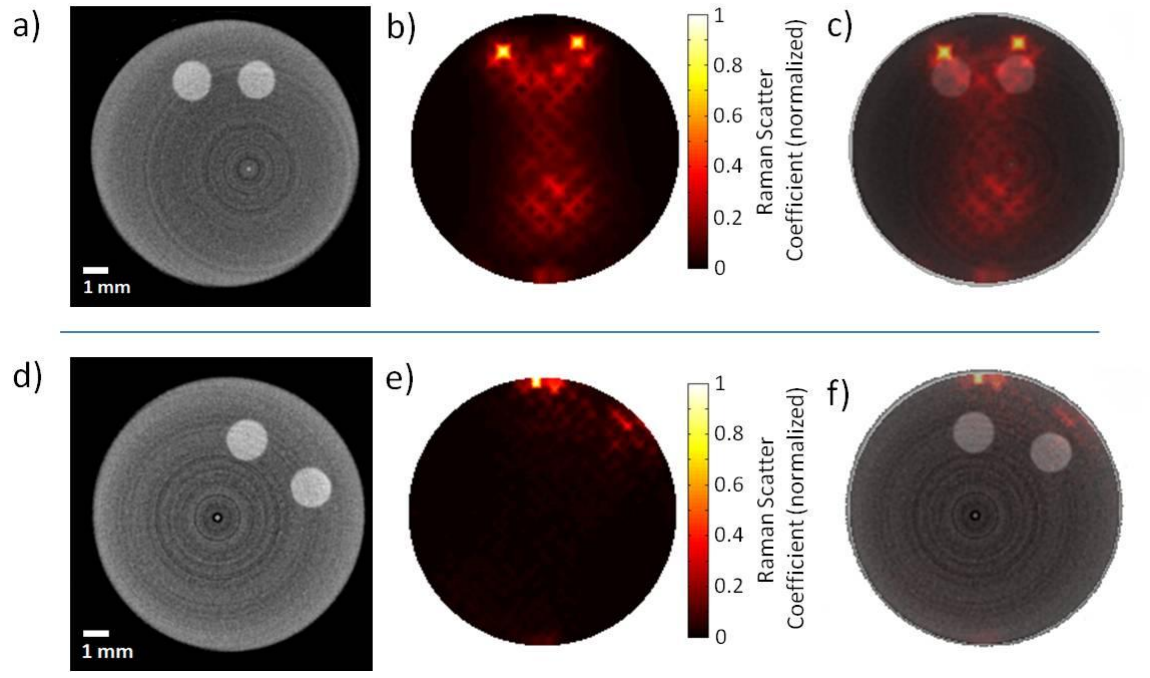

Figure 3.7. A) Micro-CT reconstruction of a phantom with two PTFE spheres (0.1% Intralipid). B) Nirfast reconstruction. C) Micro-CT and reconstruction overlay. D) Micro-CT reconstruction of a phantom with two PTFE spheres (0.5% Intralipid). E) Nirfast reconstruction. F) Micro-CT and reconstruction overlay.

Figure 3.7a shows the micro-CT reconstruction of a phantom with two small embedded PTFE spheres, illustrating their small separation relative to target size. Figure 3.7b shows the Nirfast reconstruction using data from the Raman tomography experiment. Two closely-spaced targets are predicted with some shadowing seen in the center of the reconstruction. In order to visualize the accuracy of the target sizes and positions, Figure 3.7c shows an overlay of the micro-CT reconstruction atop the Nirfast reconstruction. The error in the center position of each sphere is less than 1mm.

The 0.1% Intralipid phantoms are opaque to the eye, but have only about 1/5 the scattering power of some epithelial tissues.[9] As such, the same experiment on a phantom consisting of 0.5% Intralipid. Figure 3.7d shows the micro-CT reconstruction of the phantom, Figure 3.7e shows the Nirfast reconstruction, and Figure 3.7f shows the overlay of the two. It is immediately noticeable that the positions of the targets are not correct. Although the angular spacing between the spheres is accurate, their positions are 'projected' onto the edge of the phantom. The 'depths' of these targets cannot be resolved at this level of scattering using the current instrumentation and reconstruction methods.

Part of the inability to resolve this depth information is due to differences between the light modeling methods used (diffusion) and the actual experimental parameters. Deviations from idealized diffusion imply two major considerations for Raman spectroscopic tomography and instrument design: optimal instrumentation configuration and measurement parameters cannot be determined if accurate specimen illumination and light collection cannot be modeled, and correct reconstructions cannot be obtained if reconstruction algorithms are misinterpreting the experimental data due to the inability to accurately determine the specimen region probed for each source-detector pairing. Correcting for these differences requires reconsidering the diffusion regime and its required assumptions in favor of a modeling technique that allows for more accurate descriptions of instrument sources, detectors, and light-specimen interactions.

Ray tracing through an iterative Monte Carlo script represents a solution for light modeling that accommodates a full description of an instrument's sources, detectors, and specimens. Such a simulation models the travel of individual photons as they are generated at a source, enter, travel through, and eventually exit or become absorbed within the specimen. The path traveled is a 'random walk' governed by statistical distributions determined by user-input properties of the instrument and specimen (source placement, width, and angular distribution; specimen refractive index, mean scattering length, and mean absorbance length; detector placement, width, and numerical aperture). By recording the paths of thousands of such photons, a detailed description of how the specimen is illuminated and the distribution of collected photons is generated. The power of this approach is that it is relatively simple and straightforward to ray trace individual photons and predict their behaviors during interaction with the specimen. As there is no analytical solution for the radiative transport equation outside of the diffusion regime, a photon modeling approach represents a reasonable solution to more accurate modeling of a range of instruments and specimens.

Monte Carlo approaches are not without drawbacks. Modeling a single photon is a computationally intensive iterative process; modeling a sufficient number of photons for each source and detector can increase this computational burden by several orders of magnitude. While there have been solutions in the literature to increase computational efficiency, including modeling 'big' photons which undergo multiple absorbance events[80] and the use of graphics processing units (GPUs) for code speedup,[81] Monte Carlo methods require more computing than radiative transport calculations. Second, Monte Carlo simulations only model photon flux and absorbance events: all information pertaining to phase is lost. While this is not a drawback for Raman scattering processes, it makes the technique less appealing for modeling other optical phenomena. Additionally, simulations driven by underlying random processes do not converge on an exact solution but only approach one as more photons are modeled. Reducing this variability to an acceptable level through increased runtimes is another consideration. Despite these

computational challenges, the approach presents a fully customizable means of modeling specimen illumination and performing reconstructions from experimental data.

Table 3.1. Comparison of the three main differences between radiative transport (Nirfast) and Monte Carlo simulations. The lack of an analytical solution to radiative transport equation outside of the diffusion regime requires that photons migration mimics diffusion and that all point sources and detectors are idealized. Monte Carlo simulations do not require these assumptions, as photons can migrate outside of the diffusion regime and sources and detectors can be modeled to have small numerical apertures.

Feature comparison: Radiative Transport vs. Monte Carlo forward models

Feature	Radiative Transport + Diffusion	Monte Carlo
Photon migration	Diffusion behavior	No diffusion assumption
Source	Point sources	Directionalized (laser) illumination
Detectors	NA = 1	NA < 1

A Monte Carlo photon ray tracing code was written in-house in Matlab. The cylindrical specimen was represented by a circular mesh (similar to that used in the Nirfast reconstructions) comprised of 709 square pixels (as compared to ~1750 triangular elements in the Nirfast reconstructions), each with a defined mean scattering length, mean absorbance length, refractive index, etc. For the following discussion, fluence modeling was performed on a simulated homogeneous circular tissue phantom with 16 equally-spaced sources and detectors spread equally over the surface. This is often referred to as a

standard ‘fan’ geometry in DOT literature.[7] For the Nirfast simulations, all sources were treated as point sources, all detectors had an effective numerical aperture of one, and photon migration occurred under the assumption of the diffusion regime. These three characteristics are required for Nirfast simulations and diffusion-regime radiative transport calculations in general. In contrast, the Monte Carlo simulations utilized directionalized laser sources, small numerical aperture detectors, and a Poisson distribution to model scattering. These differences are summarized in Table 3.1. The images from the Monte Carlo simulation shown (Figure 3.8) below look significantly more ‘pixilated’ than their Nirfast counterparts because the data are not interpolated before being presented to the user.

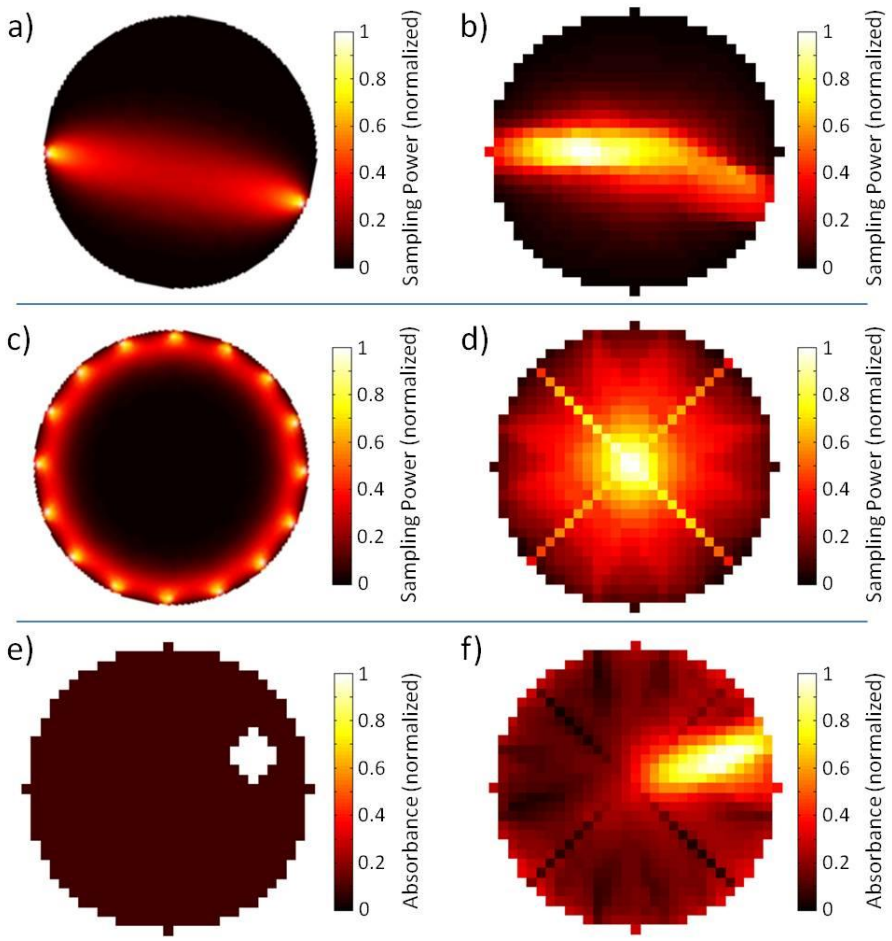

Figure 3.8. Comparison of Nirfast and Monte Carlo simulations Top: Simulation of the sampling region of a 157.5° source-detector separation in A) Nirfast and with B) Monte Carlo simulations. Middle: Total sampling region for 16 equally-spaced sources and detectors in C) Nirfast and D) Monte Carlo simulations. Bottom: E) simulated mesh showing a single absorbing region and F) the corresponding reconstruction using Monte Carlo as the forward model.

Visualizing the sampling region of a single source-detector pair using the adjoint source approximation illustrates the differences between point and directionalized sources and detectors. The adjoint source approximation, employed by both Nirfast and the Monte Carlo simulation, states that if a source and a detector switch positions the detected power will remain the same as the detected photons must travel through the same region. Simulating the fluence from a source and the fluence from a detector (as though

it were a source) and multiplying these two regions together shows the mutual 'sampling' region of the two. This approximation holds true as long as scattering is assumed to be isotropic or if the optical process bridging the two regions (spontaneous Raman scattering) is isotropic. Figure 3.8a and Figure 3.8b depict a homogeneous circular mesh with a source-detector pair at an angle of 157.5°. Using the adjoint source approximation, the effective sampling region for both a point source with a 'point' detector and a directionalized laser source with a less-than-unity numerical aperture detector are shown. The Monte Carlo simulation shows that the majority of the collected signal originates from the bulk, while in the diffusion regime the most intense signal originates from the phantom's surface. A strong preference for bulk signal agrees with previous Monte Carlo simulations regarding to transmission Raman measurements.[38] Quantitatively, the sampling power distribution of these two regions differs by approximately 23%. These differences in sampling region are more pronounced when all source-detector combinations are taken into account, representing the sampling region for an entire experiment. The results from summing the sampling regions for all 240 source-detector combinations are shown in Figure 3.8c and Figure 3.8d.

Fluence modeling simulations through Monte Carlo methods can also be used for reconstruction purposes. Using the same mesh, a region of anomalous absorbance was added (Figure 3.8e and Figure 3.8f), simulated experimental data was generated by Monte Carlo fluence modeling, and the data was supplied to a reconstruction algorithm utilizing the same Monte Carlo method and homogeneous absorbance properties for a starting guess. It should be noted that this reconstruction type is fundamentally different from those discussed in the rest of this paper, as Raman/fluorescence reconstructions investigate a photon generation process and require measured values for both the Raman signal and the fundamental frequency, while an 'absorbance' reconstruction is attenuation based and only utilizes one data point per source-detector pair. Even so, this demonstrates that Monte Carlo fluence simulations have sufficient repeatability to be useful in reconstruction algorithms. In order to maximize

this utility, processing times need to be decreased significantly, for example, through the use of graphics processing units (GPUs).

The simulation comparisons indicate that while diffuse optical tomography and Raman tomography are similar in form and function, they can differ drastically in analyte response. Radiative transport calculations have been an invaluable tool in DOT, as the results are highly reproducible and accurately model many optical setups. Upon moving to lower scattering levels, smaller sample sizes, and the use of laser sources and small-NA detectors, this becomes a less accurate model. For transmission Raman tomography, fluence modeling simulations allowing for the accurate modeling of arbitrary sources, detectors, and sample geometries will need to be realized. Monte Carlo simulations bolstered by techniques for increased computing speeds represent one possible means to this development. This study highlights the needs for such methods and provides a model to investigate the same and compare them with standard DOT reconstructions.

Section 3.4 Conclusions

A simple diffuse optical tomography-style Raman instrument in conjunction with the open-source DOT reconstruction software Nirfast can be used to determine the position of multiple Raman-scattering spheres buried in a translucent tissue phantom. The accuracy of this process is limited by the instrument's deviation from a set of ideal parameters, including very high scattering levels and non-point source illumination. While radiative transport calculations can be used as a first approximation for Raman tomography reconstructions, the two processes are fundamentally different. In order to produce the most accurate reconstructions and to design the most efficient Raman tomography instrumentation, an alternative fluence modeling method such as Monte Carlo simulation must be utilized.

CHAPTER 4: CONCLUSIONS

The untapped potential of chemical imaging for biomedical or scientific use can be realized by the development of new imaging technologies and modalities. We have presented two novel instrument designs, each of which represents initial steps towards increased utility of vibrational spectroscopy in imaging applications. The use of a QCL for DF-IR imaging may lead to increased acquisition speed when only a small number of spectroscopic bands are to be probed. Furthermore, the large flux generated by these sources allows for high-density diffraction-limited imaging of small regions of a specimen. This unique advantage may enable a point mapping imaging modality with which no current infrared technology can compete. The development of diffuse Raman tomography instrumentation explores the extrapolation of Raman imaging from two dimensions to three without the use of spatial priors. We have demonstrated that it is possible to localize collected Raman signal to regions on the order of millimeters for probing turbid media. In the case of both instruments, this thesis represents a guide for the future development of these technologies. Realizing effective widefield QCL infrared imaging will require an intimate knowledge of coherent effects coupled with scattering. We have suggested that the future development of diffuse Raman tomography instrumentation should be guided by simulations for performance optimization, and that Monte Carlo methods may provide more representative evaluations than radiative transport calculations for laser-based systems. With these considerations in place, advances in both instrumentation and theory will allow for more effective implementations of chemical imaging technology.

REFERENCES

[1] C. Matthäus, B. Bird, M. Miljković, T. Chernenko, M. Romeo, M. Diem. "Infrared and Raman Microscopy in Cell Biology". Meth. Cell Biol. 2008. 89: 275-308.

[2] A. Zoladek, F.C. Pascut, P. Patel, I. Notingher. "Non-invasive time-course imaging of apoptotic cells by confocal Raman micro-spectroscopy". J. Raman Spectrosc. 2011. 42(3): 251-258.

[3] P.J. Caspers, G.W. Lucassen, G.J. Puppels. "Combined in vivo confocal Raman spectroscopy and confocal microscopy of human skin". Biophys. J. 2003. 85(1): 572-580.

[4] V. Kumar, A.K. Abbas, N. Fausto, J.C. Aster, editors. Robbins and Cotran Pathologic Basis of Disease. Eighth edition. Saunders Elsevier, Philadelphia, PA, 2010.

[5] E. Foucar. "Do pathologists play dice? Uncertainty and early histopathological diagnosis of common malignancies". Histopathology. 1997. 31(6): 495-502.

[6] D. Gur, L.P. Wallace, A.H. Klym, L.A. Hardesty, G.S. Abrams, R. Shaha, J.H. Sumkin. "Trends in Recall, Biopsy, and Positive Biopsy Rates for Screening Mammography in an Academic Practice". Radiology. 2005. 235: 396-401.

[7] R. Bhargava "Towards a practical Fourier transform infrared chemical imaging protocol for cancer histopathology". Anal. Bioanal. Chem. 2007. 389(4): 1155-1169.

[8] J.M. Kwiatkoski, J.A. Reffner. "FT-IR microspectrometry advances". Nature. 1987. 328(27): 837-838.

[9] R. Bhargava, B.G. Wall, J.L. Koenig. "Comparison of the FT-IR mapping and imaging techniques applied to polymeric systems". Appl. Spectrosc. 2000. 54(4): 470-479.

[10] M.J. Walsh, R.K. Reddy, R. Bhargava. "Label-free Biomedical Imaging with Mid-Infrared Microspectroscopy". IEEE J. Sel. Top. Quant. 2012. 18(4): 1502-1513.

[11] C. Hirschmugl. "Infrared synchrotron radiation instrumentation and applications". Nucl. Instrum. Meth. A. 1992. 319(1-3): 245-249.

[12] S.W. Huffman, R. Bhargava, I.W. Levin. "Generalized implementation of rapid-scan Fourier transform infrared spectroscopic imaging". Appl. Spectrosc. 2002. 56(8): 965-969.

[13] C.M. Snively, S. Katzenberger, G. Oskarsdottier, J. Lauterbach. "Fourier-transform infrared imaging using a rapid-scan spectrometer". Opt. Lett. 1999. 24(24): 1841-1843.

[14] R. Bhargava, I.W. Levin. “Fourier transform mid-infrared spectroscopic imaging: Microspectroscopy with multichannel detectors”. In: R. Bhargava, I.W. Levin, editors. Spectrochemical Analysis using Infrared Multichannel Detectors. Blackwell Publishing Ltd., 2005. 1-24.

[15] D.L. Elmore, M.W. Tsao, S. Frisk, D.B. Chase, J.F. Rabolt. “Design and performance of a planar array infrared spectrograph that operates in the 3400 to 2000 cm^{-1} region”. Appl. Spectrosc. 2002. 56(2): 145-149.

[16] J.N. Liu, M.V. Schulmerich, R. Bhargava, B.T. Cunningham. “Optimally designed narrowband guided-mode resonance reflectance filters for mid-infrared spectroscopy”. Opt. Exp. 2011. 19(24): 24182-24197.

[17] B. Lendl, R. Schindler. “Flow-through sensors for enhancing sensitivity and selectivity of FTIR spectroscopy in aqueous media”. Vib. Spectrosc. 1999. 19(1): 1-10.

[18] P.R. Griffiths, J.A. De Haseth, editors. Fourier Transform Infrared Spectrometry. Second edition. Wiley-Interscience, 2007.

[19] H.N. Holman, M.C. Martin, E.A. Blakey, K. Bjornstad, W.R. McKinney. “IR spectroscopic characteristics of cell cycle and cell death probed by synchrotron radiation based Fourier transform IR spectromicroscopy”. Biopolymers. 2000. 57(6): 329-335.

[20] M.J. Nasse, R. Reininger, T. Kubala, S. Janowski, C. Hirschmugl. “Synchrotron infrared microspectroscopy imaging using a multi-element detector (IRMSI-MED) for diffraction-limited chemical imaging”. Nucl. Instrum. Meth. A. 2007. 582(1): 107-110.

[21] A.K. Kodali, M. Schulmerich, J. Ip, G. Yen, B.T. Cunningham, R. Bhargava. “Narrowband midinfrared reflectance filters using guided mode resonance”. Anal. Chem. 2010. 82(13): 5697-5706.

[22] J. Faist, F. Capasso, D.L. Sivco, C. Sirtori, A.L. Hutchinson, A.Y. Cho. “Quantum Cascade Laser”. Science. 1994. 264(5158): 553-556.

[23] A.A. Kosterev, F.K. Tittel. “Chemical Sensors Based on Quantum Cascade Lasers”. IEEE J. Quantum Electron. 2002. 38(6): 582-591.

[24] K. Namjou, S. Cai, E.A. Whittaker, J. Faist, C. Gmachl, F. Capasso, D.L. Sivco, A.Y. Cho. “Sensitive absorption spectroscopy with a room-temperature distributed-feedback quantum-cascade laser”. Opt. Lett. 1998. 23(3): 219-223.

[25] B.A. Paldus, T.G. Spence, R.N. Zare, J. Oomens, F.J.M. Harren, D.H. Parker, C. Gmachl, F. Cappasso, D.L. Sivco, J.N. Baillargeon, A.L. Hutchinson, A.Y. Cho. “Photoacoustic spectroscopy using quantum-cascade lasers”. Opt. Lett. 1999. 24(3): 178-180.

[26] M.J. Weida, P.R. Buerki, M. Pushkarsky, T. Day. “QCL-assisted infrared chemical imaging”. Micro- and Nanotechnology Sensors, Systems, and Applications. 2011. 8031: 803127.

[27] M. Brandstetter, A. Genner, K. Anic, B. Lendl. “Tunable Mid-IR lasers: A new avenue to robust and versatile physical chemosensors”. Procedia Eng. 2010. 5: 1001-1004.

[28] R. Reddy, B. Davis, P.S. Carney, R. Bhargava. “Modeling Fourier transform infrared spectroscopic imaging of Prostate and Breast Cancer tissue specimens”. IEEE I. S. Biomed. Imaging. 2011. 738-741.

[29] A.S. Haka, I.W. Levin, E.N. Lewis. “Uncooled barium strontium titanium focal plane array detection for mid-infrared Fourier transform spectroscopic imaging”. Appl. Spectrosc. 2000. 54(5): 753-755.

[30] R. Bhargava. “Infrared spectroscopic imaging: the next generation”. Appl. Spectrosc. 2012. Submitted.

[31] H. Amrania, A. McCrow, C. Phillips. “A Benchtop Ultrafast Infrared Spectroscopic Imaging System for Biomedical applications”. Rev. Sci. Instrum. 2009. 80: 123702.

[32] B.J. Davis, P.S. Carney, R. Bhargava. “Theory of mid-infrared absorption microspectroscopy. II. Heterogeneous samples”. Anal. Chem. 2010. 82: 3487–3499.

[33] B.J. Davis, P.S. Carney, R. Bhargava. “Theory of mid-infrared absorption microspectroscopy. I. Homogeneous samples”. Anal. Chem. 2010. 82: 3474–3486.

[34] B.J. Davis, P.S. Carney, R. Bhargava. “Infrared Microspectroscopy of Intact Fibers”. Anal. Chem. 2011. 83: 525–532.

[35] R.K. Reddy, M.J. Walsh, M.V. Schulmerich, P.S. Carney, R. Bhargava. “High-definition infrared spectroscopic imaging”. Appl. Spectrosc. 2012. In press.

[36] R. Bhargava. “Fellgett advantage in Fourier transform infrared imaging”. Under preparation.

[37] S. Schaden, M. Haberkorn, J. Frank, J.R. Baena, B. Lendl. “Direct determination of carbon dioxide in aqueous solution using mid-infrared quantum cascade lasers”. Appl. Spectrosc. 2004. 58(6): 667-670.

[38] M.J. Nasse, M.J. Walsh, E.C. Mattson, R. Reininger, A. Kajdacsy-Balla, V. Macias, R. Bhargava, C.J. Hirschmugl. “High-resolution Fourier transform infrared chemical imaging with multiple synchrotron beams”. Nat. Methods. 2011. 8: 413-416.

[39] P. Dumas, G.L. Carr, G.P. Williams. "Enhancing the lateral resolution in infrared microspectrometry by using synchrotron radiation: Applications and perspectives". Analusis. 2000. 28(1): 68-74.

[40] N. Jamin, P. Dumas, J. Moncuit, W-H. Fridman, J-L. Teillaud, G.L. Carr, G.P. Williams. "Highly resolved chemical imaging of living cells by using synchrotron infrared microspectrometry". Proc. Nat. Acad. Sci. USA. 1998. 95(9): 4837-4840.

[41] L.M. Miller, R.J. Smith. "Synchrotrons versus globars, point-detectors versus focal plane arrays: Selecting the best source and detector for specific infrared microspectroscopy and imaging applications". Vib. Spectrosc. 2005. 38(1-2): 237-240.

[42] H. Obrigh, A. Villringer. "Beyond the visible – imaging the human brain with light". J. Cereb. Blood Flow Metab. 2003. 23: 1-18.

[43] J.C. Hebden, D.T. Delpy. "Diagnostic Imaging with light". Br. J. Radiol. 1997. 70: S206-S214.

[44] R.F. Bonner, R. Nossal, S. Havlin, G.H. Weiss. "Model for photon migration in turbid biological media". J. Opt. Soc. Am. A. 1987. 4(3): 423-432.

[45] D. Contini, F. Martelli, G. Zaccanti. "Photon migration through a turbid slab described by a model based on diffusion approximation. I. Theory". Appl. Opt. 1997. 36(19): 4587-4599.

[46] M. Schweiger, S.R. Arridge, I. Nissila. "Gauss-Newton method for image reconstruction in diffuse optical tomography". Phys. Med. Biol. 2005. 50(10): 2365-2386.

[47] M. Schweiger, A. Gibson, S.R. Arridge. "Computational Aspects of Diffuse Optical Tomography". Comput. Sci. Eng. 2003. 5(6): 33-41.

[48] B.W. Pogue, T.O. McBride, U.L. Osterberg, K.D. Paulsen. "Comparison of imaging geometries for diffuse optical tomography of tissue". Opt. Express. 1999. 4(8): 270-286.

[49] B.A. Brooksby, H. Dehghani, B.W. Pogue, K.D. Paulesn. "Near-infrared (NIR) tomography breast image reconstruction with a priori structural information from MRI: Algorithm development for reconstructing heterogeneities". IEEE J. Sel. Top. Quantum Electron. 2003. 9(2): 199-209.

[50] B.W. Pogue, S.P. Poplack, T.O. McBride, W.A. Wells, K.S. Osterman, U.L. Osterberg, K.D. Paulsen. "Quantitative hemoglobin tomography with diffuse near-infrared spectroscopy: Pilot results in the breast". Radiology. 2001. 218(1): 261-266.

[51] V. Ntziachristos, B. Chance. "Probing physiology and molecular function using optical imaging: Applications to breast cancer". Breast Cancer Res. 2001. 3(1): 41-46.

[52] D.A. Boas, T. Gaudette, G. Strangman, X. Cheng, J.J.A. Marota, J.B. Mandeville. "The accuracy of near infrared spectroscopy and imaging during focal changes in cerebral hemodynamics". NeuroImage. 2001. 13(1): 76-90.

[53] A.H. Hielscher. “Optical tomographic imaging of small animals”. Curr. Opin. Biotechnol. 2005. 16(1): 79-88.

[54] A.P. Gibson, J.C. Hebden, S.R. Arridge. “Recent advances in diffuse optical imaging”. Phys. Med. Biol. 2005. 50: R1-R43.

[55] B. Chance, M. Cope, E. Gratton, N. Ramirez, B.J. Tromberg. “Phase measurement of light absorption and scatter in human tissue”. Rev. Sci. Instrum. 1998. 69: 3457-3481.

[56] J.C. Hebden, S.R. Arridge, D.T. Delpy. “Optical imaging in medicine: I. Experimental techniques”. Phys. Med. Biol. 1997. 42: 825-840.

[57] M.A. O’Leary, D.A. Boas, B. Chance, A.G. Yodh. “Experimental images of heterogeneous turbid media by frequency-domain diffusing-photon tomography”. Opt. Lett. 1995. 20(5): 426-428.

[58] A. Li, E.L. Miller, M.E. Kilmer, T.J. Brukilacchio, T. Chaves, J. Scott, Q. Zhang, T. Wu, M. Chorlton, R.H. Moore, D.B. Kopans, D.A. Boas.“Tomographic optical breast imaging guided by three-dimensional mammography”. Appl. Opt. 2003. 42(25): 5181-5190.

[59] A. Corlu, T. Durduran, R. Choe, M. Schweiger, E.M.C. Hillman, S.R. Arridge, A.G. Yodh. “Uniqueness and wavelength optimization in continuous-wave multispectral diffuse optical tomography”. Opt. Lett. 2003. 28: 2339-2341.

[60] N. Shah, A.E. Cerussi, D. Jakubowski, D. Hsiang, J. Butler, B.J. Tromberg. “Spatial variations in optical and physiological properties of healthy breast tissue”. J. Biomed. Opt. 2004. 9(3): 534-540.

[61] V. Ntziachristos, B. Chance. “Probing physiology and molecular function using optical imaging: applications to breast cancer”. Breast Cancer Res. 2001. 3: 41-46.

[62] D.L. Wetzel. “Chemical Sensing Using Near-IR Reflectance Analysis”. In: D. Schuetzle, R. Hammerle, editors. Fundamentals and Applications of Chemical Sensors. American Chemical Society, 1986. 271-296.

[63] P. Matousek, I.P. Clark, E.R.C. Draper, M.D. Morris, A.E. Goodship, N. Everall, M. Towrie, W.F. Finney, A.W. Parker. “Subsurface probing in diffusely scattering media using spatially offset Raman spectroscopys”. Appl. Spec. 2005. 4: 393-400.

[64] P. Matousek. “Inverse spatially offset Raman spectroscopy for deep noninvasive probing of turbid media”. Appl. Spec. 2006. 60(11): 1341-1347.

[65]M.V. Schulmerich, K.A. Dooley, T.M. Vanasse, S.A. Goldstein, M.D. Morris. “Subsurface and transcutaneous Raman spectroscopy and mapping using concentric illumination rings and collection with a circular fiber-optic array”. Appl. Spec. 2007. 61(7): 671-678.

[66] M.V. Schulmerich, J.H. Cole, J.M. Kreider, F. Esmonde-White, K.A. Dooley, S.A. Goldstein, M.D. Morris. "Transcutaneous Raman spectroscopy of murine bone in vivo". Appl. Spec. 2009. 63(3): 286-295.

[67] M.V. Schulmerich, W.F. Finney, R.A. Fredricks, M.D. Morris. "Subsurface Raman spectroscopy and mapping using a globally illuminated non-confocal fiber-optic array probe in the presence of Raman photon migration". Appl. Spec. 2006. 60(2): 109-114.

[68] M.V. Schulmerich, M.D. Morris, T.M. Vanasse, S.A. Goldstein. "Transcutaneous Raman spectroscopy of bone global sampling and ring/disk fiber optic probes". Pro. Biomed. Opt. Imag. 2007. 6430: 643009.

[69] S. Srinivasan, M.V. Schulmerich, B.W. Pogue, M.D. Morris. "3-D Image-guided Raman Characterization in a Phantom Study". J. Biomed. Opt., OSA Technical Digest (CD) (Optical Society of America). 2008. BWD5.

[70] S. Srinivasan, M. Shulmerich, J.H. Cole, K.A. Dooley, J.M. Kreider, B.W. Pogue, M.D. Morris, S.A. Goldstein. "Image-guided Raman sepectroscopic recovery of canine cortical bone contrast in situ". Opt. Express. 2008. 16(16): 12190-12200.

[71] S.T. Flock, S.L. Jacques, B.C. Wilson, W.M. Star, M.J.C van Gemert. "Optical Properties of Intralipid: A Phantom Medium for Light Propagation Studies". Laser. Surg. and Med. 1992. 12: 510-519.

[72] J.R. Mourant, T. Fuselier, J. Boyer, T.M. Johnson, I.J. Bigio. "Predictions and measurements of scattering and absorption over broad wavelength ranges in tissue phantoms". App. Opt. 1997. 36(4): 949-957.

[73] R. Cubeddu, A. Pifferi, P. Taroni, A. Torricelli, G. Valentini. "A solid tissue phantom for photon migration studies". Phys. Med. Biol. 1997. 42(10): 1971-1979.

[74] T. Collier, D. Arifler, A. Malpica, M. Follen, R. Richards-Kortum. "Determination of Epithelial Tissue Scattering Coefficient Using Confocal Microscopy". IEEE J. Sel. Top. Quantum Electron. 2003. 9(2): 307-313.

[75] T. Durduran, R. Choe, J.P. Culver, L. Zubkov, M.J. Holboke, J. Giammarco, B. Chance, A.G. Yodh. "Bulk optical properties of healthy female breast tissue". Phys. Med. Biol. 2002. 47(16): 2847-2861.

[76] C.A. Thompson, J.S. Reynolds, K.J. Webb. "Raman spectroscopic studies of diamond in Intralipid". Opt. Lett. 1995. 20(10): 1195-1197.

[77] J.H. Siewerdsen, D.A. Jaffray. "Optimization of x-ray imaging geometry (with specific application to flat-panel cone-beam computed tomography)". Med. Phys. 2000. 27(8): 1903-1914.

[78] H. Dehghani, M.E. Eames, P.K. Yalavarthy, S.C. Davis, S. Srinivasan, C.M. Carpenter, B.W. Pogue, K.D. Paulsen. "Near infrared optical tomography using NIRFAST: Algorithm for numerical model and image reconstruction". Commun. Numer. Meth. Engng. 2008. 25(6): 711-732.

[79] N. Everall, I. Priestnall, P. Dallin, J. Andrews, I. Lewis, K. Davis, H. Owen, M.W. George. "Measurement of Spatial Resolution and Sensitivity in Transmission and Backscattering Raman Spectroscopy of Opaque Samples: Impact on Pharmaceutical Quality Control and Raman Tomography". Appl. Spec. 2010. 64(5): 476-484.

[80] L.H. Wang, S.L. Jacques, L.Q. Zheng. "Mcml monte carlo modeling of light transport in multilayered tissues". Comput. Meth. Prog. Bio. 1995. 47(2): 131-146.

[81] E. Alerstam, T. Svensson, S. Andersson-Engels. "Parallel computing with graphics processing units for high-speed monte carlo simulations of photon migration". J. Biomed. Opt. 2008. 13(6): 060504.